



Troloxerutin-Mediated Complement Pathway Inhibition is a Disease-Modifying Treatment for Inflammatory Arthritis

Debasis Sahu^{1,2*}, Subasa Chandra Bishwal^{3†}, Md. Zubair Malik⁴, Sukanya Sahu³, Sandeep Rai Kaushik³, Shikha Sharma⁵, Ekta Saini⁶, Rakesh Arya³, Archana Rastogi⁷, Sandeep Sharma⁸, Shanta Sen¹, R. K. Brojen Singh⁴, Chuan-Ju Liu², Ranjan Kumar Nanda^{3*} and Amulya Kumar Panda^{1*}

OPEN ACCESS

Edited by:

Jiake Xu,
University of Western Australia,
Australia

Reviewed by:

Jyoti Sharma,
Institute of Bioinformatics (IOB), India
Sadiq Umar,
University of Illinois at Chicago,
United States

*Correspondence:

Debasis Sahu
debasissahu.phd@gmail.com
Ranjan Kumar Nanda
ranjan@icgeb.res.in
Amulya Kumar Panda
amulya@nii.res.in

†Present address:

Subasa Chandra Bishwal,
National Institute of Research in Tribal
Health, Jabalpur, India

Specialty section:

This article was submitted to
Stem Cell Research,
a section of the journal
Frontiers in Cell and Developmental
Biology

Received: 29 December 2021

Accepted: 03 March 2022

Published: 31 March 2022

Citation:

Sahu D, Bishwal SC, Malik MZ,
Sahu S, Kaushik SR, Sharma S,
Saini E, Arya R, Rastogi A, Sharma S,
Sen S, Singh RKB, Liu C-J, Nanda RK
and Panda AK (2022) Troloxerutin-
Mediated Complement Pathway
Inhibition is a Disease-Modifying
Treatment for Inflammatory Arthritis.
Front. Cell Dev. Biol. 10:845457.
doi: 10.3389/fcell.2022.845457

¹Product Development Cell, National Institute of Immunology, New Delhi, India, ²Department of Orthopedics Surgery, New York University School of Medicine, New York, NY, United States, ³Translational Health Group, International Centre for Genetic Engineering and Biotechnology (ICGEB), New Delhi, India, ⁴School of Computational & Integrative Sciences, Jawaharlal Nehru University, New Delhi, India, ⁵Amity Institute of Forensic Sciences, Amity University, Noida, India, ⁶Malaria Group, International Centre for Genetic Engineering and Biotechnology (ICGEB), New Delhi, India, ⁷Department of Pathology, Institute of Liver and Biliary Sciences, New Delhi, India, ⁸Department of Medical Laboratory Sciences, Lovely Professional University, Phagwara, India

Troloxerutin (TXR) is a phytochemical reported to possess anti-inflammatory and hepatoprotective effects. In this study, we aimed to exploit the antiarthritic properties of TXR using an adjuvant-induced arthritic (AIA) rat model. AIA-induced rats showed the highest arthritis score at the disease onset and by oral administration of TXR (50, 100, and 200 mg/kg body weight), reduced to basal level in a dose-dependent manner. Isobaric tags for relative and absolute quantitative (iTRAQ) proteomics tool were employed to identify deregulated joint homogenate proteins in AIA and TXR-treated rats to decipher the probable mechanism of TXR action in arthritis. iTRAQ analysis identified a set of 434 proteins with 65 deregulated proteins (\log_2 case/control ≥ 1.5) in AIA. Expressions of a set of important proteins (AAT, T-kininogen, vimentin, desmin, and nucleophosmin) that could classify AIA from the healthy ones were validated using Western blot analysis. The Western blot data corroborated proteomics findings. *In silico* protein-protein interaction study of tissue-proteome revealed that complement component 9 (C9), the major building blocks of the membrane attack complex (MAC) responsible for sterile inflammation, get perturbed in AIA. Our dosimetry study suggests that a TXR dose of 200 mg/kg body weight for 15 days is sufficient to bring the arthritis score to basal levels in AIA rats. We have shown the importance of TXR as an antiarthritic agent in the AIA model and after additional investigation, its arthritic ameliorating properties could be exploited for clinical usability.

Keywords: troloxerutin, adjuvant induced arthritis, iTRAQ, proteomics, anti-inflammatory, antioxidant

1 INTRODUCTION

Rheumatoid arthritis (RA) is a chronic, systemic autoimmune inflammatory disorder primarily affecting the synovial joints with concomitant destruction of joint tissues. Almost 1% of the world population irrespective of race and region is suffering from RA with its preponderance more in women than in men (Guo et al., 2018). Commonly used anti-tumor necrosis factor (TNF) drugs

provide relief to only about 60% of RA patients. Interleukin (IL)-6 is also one such inflammatory mediator which plays a major role in arthritis. The biological inhibitor of IL-6, tocilizumab, is being used to treat RA (Biggioggero et al., 2019). Long-term use of nonsteroidal anti-inflammatory drugs (NSAIDs) such as diclofenac sodium to manage RA leads to persistent adverse events (Crofford, 2013). Therapeutic advances have significantly improved the lives of RA patients, but the problem needs additional solutions to resolve the clinical issues associated with this disease. Identification of alternative drugs with minimal toxicity is the need of the hour. Plant-based extracts and phytochemicals have been used as rich sources of anti-RA agents (Islam et al., 2016; Aravilli et al., 2017; Jannat et al., 2019).

Troloxerutin (TXR), also known as vitamin P4, is a flavonoid found in cereal, coffee, tea, and many vegetables/fruits and is reported to have a wide range of pharmacological properties (Zhang et al., 2009; Thomas et al., 2017). TXR protects oxidative damage of cell membranes of neutrophils, DNA damage caused by gamma radiations, and renal and hepatic conditions. TXR reduces capillary fragility and unusual leakage, thus improving their function. It is reported to possess fibrinolytic, antithrombotic, rheological, and edema-protective activity (Maurya et al., 2005). TXR has also been used to treat chronic venous insufficiency (CVI) (Zhang et al., 2009; Panat et al., 2016).

In this study, we monitored the antioxidant potential of TXR in an *in vitro* system and to decipher its arthritic ameliorating potential, adjuvant-induced arthritis (AIA) model of the rat was used for monitoring the morphological, histological, radiological, and biochemical parameters. A global quantitative proteomics study was employed to identify the deregulated proteins in the affected synovial joint homogenate isolated from AIA rats and those receiving TXR treatment and validated using Western blot analysis. The identified joint homogenate proteins were mapped to identify interacting partners and used to predict the mechanism of TXR action. This study successfully demonstrated the importance of phytochemicals like TXR as an anti-arthritic agent and elucidated its mode of action to develop translatable solutions for difficult debilitating disease conditions like RA.

2 METHODOLOGY

2.1 Cell Culture

Murine macrophage cell-line (RAW264.7) was cultured using RPMI 1640 (Gibco, USA) medium supplemented with glutamine (2 mM), antibiotics (streptomycin: 100 µg/ml, amphotericin-B: 0.25 µg/ml, and penicillin: 100 U/ml), and fetal bovine serum (heat-inactivated, 10%) in a humidified CO₂ incubator maintained at 37°C. Varied TXR concentrations (5.2–674 µM) were introduced to RAW264.7 cells with controls, for 24 h. Trypan blue (0.4% in phosphate-buffered saline: PBS) exclusion method was used to determine cell viability in TXR-treated cells. Cytotoxicity was measured using MTT colorimetric

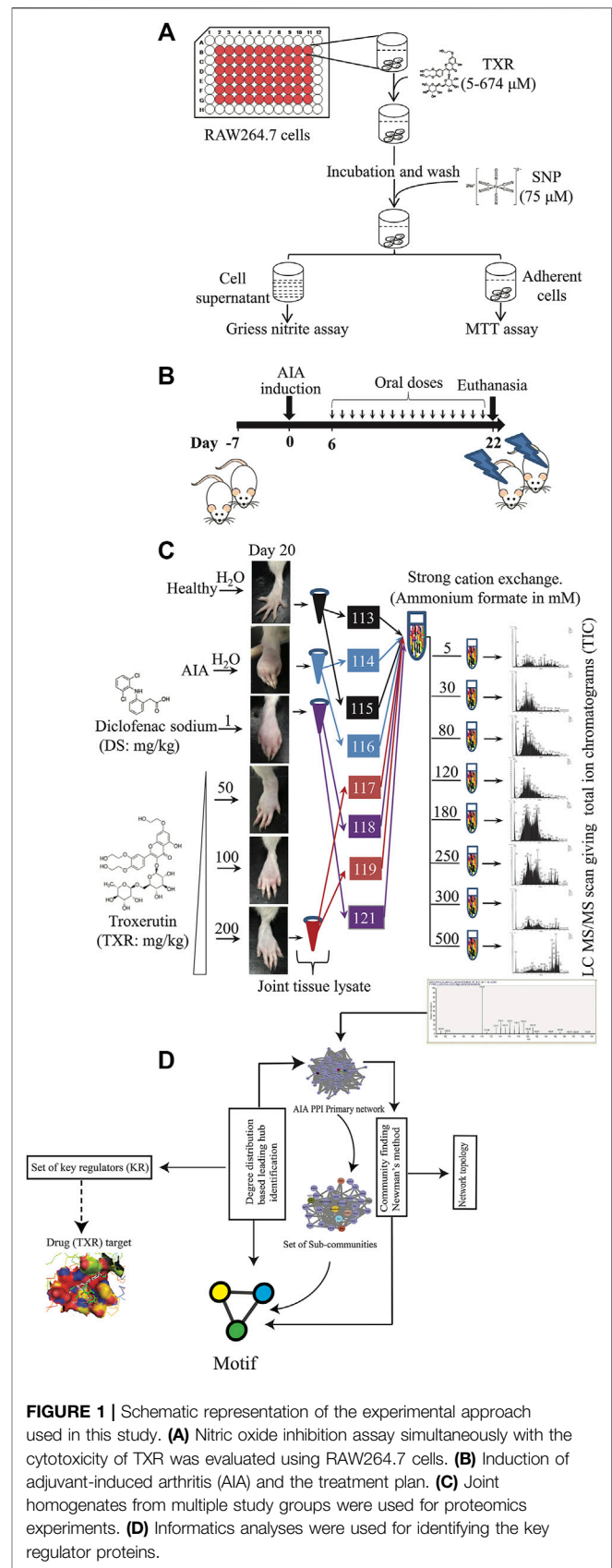


FIGURE 1 | Schematic representation of the experimental approach used in this study. **(A)** Nitric oxide inhibition assay simultaneously with the cytotoxicity of TXR was evaluated using RAW264.7 cells. **(B)** Induction of adjuvant-induced arthritis (AIA) and the treatment plan. **(C)** Joint homogenates from multiple study groups were used for proteomics experiments. **(D)** Informatics analyses were used for identifying the key regulator proteins.

assay (SigmaAldrich, USA), and Griess-nitrite assay (SigmaAldrich, USA) was carried out to measure nitric oxide production with sodium nitroprusside (SNP, 75 μ M, Sigma Aldrich, USA) as reported earlier with minor modifications (Sahu et al., 2017).

2.2 Animal Experiments

All animal experiments were performed following approved protocols by the Institutional Animal Ethics Committee (IAEC) of the National Institute of Immunology (NII), New Delhi (IAEC#367/15). Female Wistar rats, aged 6–8 weeks, were maintained at controlled temperature ($24 \pm 3^\circ\text{C}$) and humidity ($50 \pm 5\%$) with 12 h light and dark cycles; and had access to food and water *ad libitum*. After a period of acclimatization (7 days) in the animal house, study animals were randomly divided into six groups ($n = 5/\text{group}$). A schematic diagram depicting the experimental procedures adopted in this study is presented in **Figures 1A–D**. Except for the healthy control groups, the rest five groups were immunized with complete Freund's adjuvant (CFA; 100 μ l, Chondrex, USA) by intradermal injection in the subplantar region of both hind footpads. Post-CFA administration, animals were monitored for 24–36 h, and the footpad thickness was recorded using digital Vernier calipers (Mitutoyo, Japan). These animals were divided into the following groups (vehicle control:AIA, diclofenac sodium control (1 mg/kg DS), and different doses of TXR (50 mg/kg: TXR 50; 100 mg/kg: TXR 100 and 200 mg/kg: TXR 200) administered orally once a day for 15 days. Body weights of experimental animals were recorded every third-day post-AIA induction till euthanasia and the difference in mean body weight at two representative days (Islam et al., 2016; Blondel et al., 2008) was calculated. Using retro-orbital puncture, blood samples (~ 0.5 ml) were collected on day 20. After euthanizing the animals, their hind limbs were harvested for x-ray imaging, histology, and proteomic studies. Harvested kidneys and livers were fixed in formalin (10% v/v in phosphate-buffered saline: PBS) for histopathological analyses. For radiological evaluation, the right hind-limbs of each experimental animal from all study groups were fixed in formalin (10% v/v in PBS). Joint tissues excised from the left hind limbs of the animals were snap-frozen to store at -80°C for further analysis.

Prior to histology, anteroposterior roentgenograms were recorded on x-ray films using MBR-1505R (Hitachi Medical Corporation, Tokyo, Japan) at 30 kV, 6 mA, and 45 s exposure with a 50 cm distance between the X-ray source and film. The severity of bone erosion was ranked according to the Larsen scoring method with minor modifications. A score of zero (0) was assigned to normal joints and bones, while a slight abnormality in any one or both exterior metatarsal bones exhibiting minor bone erosion was scored as 1. An image with distinct abnormality in any of the metatarsal or tarsal joints having bone erosion was scored 2. Score 3 indicates medium destructive abnormalities in the metatarsal bones or tarsal bones (one or both) showing definite bone erosions. A severe destructive abnormality in all the metatarsal bones showed definite erosion involving at least one of the tarsometatarsal joints entirely eroded, but some bony joint outlines were partly preserved and scored as 4. The highest

score was 5, assigned to the severely damaged states with mutilating abnormality with no bony outlines (Seeuws et al., 2010).

After the radiological assay, the knee joint was separated out from the formalin-fixed limb by removing the skin and overlying muscles for the histological analysis. Decalcification was carried out in nitric acid (5%) incubated for 10 days prior to paraffin block preparation. Tissue sections (5 μ m) were prepared using a microtome (Leica Biosystems, Germany), stained with hematoxylin and eosin (H-E) before capturing images using a light microscope (Nikon, USA) (Sahu et al., 2015).

2.3 Histological Analysis of Liver, Kidney, and Tibiotarsal Joints

Fixed liver and kidney tissues were sectioned (8 μ m) using a rotary microtome (Leica Biosystems, Germany) and stained with H-E staining for visualization. For the histological analysis of the liver, the following parameters were considered for the eosinophilic infiltration assay. The scoring was done according to the eosinophils counted per frame of the photomicrograph. Score 0 was given if the eosinophils were absent, with 1–2 eosinophils were scored as 1. Score 2 was assigned for ≥ 3 but < 6 eosinophil count, and the highest score of 3 was assigned for eosinophilic count ≥ 6 . Semiquantitative scores (0–3) represent an average of 3 highest values of eosinophils, counted in at least 8 portal/periportal spaces. The histological scoring for the tibiotarsal joints and other soft tissues (liver and kidneys) was performed by a clinical pathologist using a standardized method (Sarin et al., 2014; Tarantino et al., 2009).

2.4 Measurement of Nitrite in Plasma

Blood (~ 0.5 ml) was drawn from rats by cardiac puncture immediately after euthanasia and collected in EDTA-coated vacutainers (Greiner Bio-One) for plasma nitrite estimation. Blood plasma was separated by centrifugation at 2,000 g for 10 min at 4°C before storing at -80°C until further analysis. Briefly, plasma (0.1 ml) and varied concentrations of sodium nitrite (100–1,562 μ M) were taken in a 96-well microtiter plate and Griess reagent (0.1 ml, Sigma Inc., USA) was added to the mixture. The reaction mixture was incubated for 10 min in the dark before measuring the absorbance at 540 nm using a spectrophotometer (Molecular devices, USA). All the samples were measured in duplicates to quantify the nitrite levels (Sharma et al., 2011).

2.5 Assessment of Arthritis Score at Disease Onset and During Treatment

Every third day, the arthritic score of all the experimental animals was recorded by a coauthor blinded to the study groups. Each experimental rat was given a score in the range of 0–4; where “0” shows no symptoms and “4” being the most severe. Combined scores of both the hind limbs were used for analysis. The paw diameters were measured every third day from the date of AIA induction (day 0) to the date of euthanasia (day 21) to calculate the arthritis index (AI) using **Equation 1** (Coelho et al., 2004).

$$\text{Arthritis index (AI \%)} = \frac{\text{Footpad thickness of experimental rat} - \text{Footpad thickness of control rat}}{\text{Footpad thickness of control rat}} \times 100 \quad (1)$$

2.6 Proteome Analysis of Arthritic Tissues

After clearing the skin and extra muscles, in the presence of liquid nitrogen, the joint tissues were pulverized to powder form using a pestle and mortar. The homogenized joint tissue samples (~500 mg each) were suspended in protein extraction buffer (50 mM Tris-HCl, pH 7.4, 1 mM PMSF and protease inhibitor cocktail; Sigma, USA Cat# P8340) for 30 min in ice before centrifuging at 4°C at 10,000 g for 10 min. The supernatant was used for estimating protein following Bradford's method (5000006, Bio-Rad, USA). An equal amount of joint homogenate protein (100 µg) from each study group was precipitated in acetone (1/6 v/v) overnight and centrifuged at 12,000 g for 20 min at 4°C to collect the pellet. The protein pellet was dissolved in a dissolution buffer and denaturant supplied with the isobaric tag for relative and absolute quantification (iTRAQ) reagent kit (AB Sciex, USA) (**Supplementary Figure S1A**). Equal quantities of proteins from all the groups were separated on a gel and a silver-stained gel image is presented in **Supplementary Figure S1B**. Supplier's protocol was followed for iTRAQ labeling. Briefly, a reducing reagent (2 µl) was added to each protein sample (100 µg) and incubated at 60°C for 1 h followed by the addition of cystine blocking reagent (1 µl). Tryptic peptides were generated by incubating the processed proteins with trypsin (20 µl) followed by overnight incubation at 37°C and dried using a vacuum evaporator (CentriVap concentrator, Labconco, USA) at 40°C for 35 min. The tryptic peptides were resuspended in a dissolution buffer, and appropriate iTRAQ tags were used for labeling the tryptic peptides by incubating for 2 h at room temperature (**Supplementary Figure S1**). Pooled iTRAQ labeled peptides were dried using SpeedVac at 40°C and an aliquot (~300 µg tryptic iTRAQ labeled peptides) was taken for strong cation exchange chromatography (SCX). Briefly, the labeled peptides were dissolved in 2 ml of SCX buffer A (5 mM ammonium formate in 30% acetonitrile, pH 2.7) and loaded onto a pre-equilibrated SCX column ICAT™ cartridge kit (AB Sciex, USA). Peptides were eluted into 8 fractions using ammonium formate buffer (pH 2.7) of different concentrations (30, 80, 120, 180, 250, 300, 400, and 500 mM). Fractions derived from the 30 and 80 mM concentrations were combined and the rest 6 peptide fractions were separately dried in the CentriVap concentrator at 40°C. These fractions were subjected to cleaning up using Pierce C18 Spin Columns (89870, ThermoFisher, USA).

2.6.1 LC MS/MS Data Acquisition

Each cleaned-up fraction was taken for reverse-phase separation coupled to an online mass spectrometer for data acquisition. Briefly, the peptide fractions (~20 µg) were dissolved in 20 µl solvent A (5% acetonitrile with 0.1% formic acid) of which 2 µl (2 µg) was injected into a precolumn and separated on a 10 cm C₁₈ Pico Frit analytical column, HypersilGold 5µ, 15-micron tip with an internal ID of 75 microns (PF7515-100H-070-36, New

Objective, USA). In a nano-LC-MS column (Thermo Fisher Scientific, USA), the peptides were separated *via* a constant flow rate of 300 nl/min with a mixture of solvent A and solvent B (95% acetonitrile with 0.1% formic acid) to achieve a solvent gradient of 5%–38% acetonitrile in 70 min, then up to 76% acetonitrile from 70 to 80 min and maintained until the completion of the 120 min run time. Mass spectrometer data acquisition was carried out using a Linear Trap Quadrupole (LTQ) Orbitrap Velos mass spectrometer (Thermo Fisher Scientific, USA). The eluates of nano-LC were directly sampled *via* an integrated electrospray emitter operating at 2.0 kV. The full-scan (m/z: 200–2,000 MS spectra) data were acquired in the positive ion mode with 10 (Panat et al., 2016) data-dependent collision-induced dissociation (CID)—higher-energy collisional dissociation (HCD) dual MS/MS scans per full scan using Fourier transform mass spectrometry (FTMS) mass analyzer; CID scans were obtained in LTQ with two-microscan averaging; HCD scans and full scans were acquired in the Orbitrap at a resolution of 15,000 and 60,000, respectively; normalized collision energy (NCE) was of 40% in HCD and 35% in CID; ±2.0 m/z isolation window; and the dynamic exclusion for 60s. In CID–HCD dual scan, selected parent ions were fragmented by CID followed by HCD. The peptides with charged states of +2 or more were considered for MS/MS fragmentation. The 10 major high abundant peptides, with 500 and above signal threshold count were selected for MS/MS and excluded dynamically for 30 milliseconds.

2.6.2 Protein Identification and Quantification:

All the mass spectrometric raw data files were analyzed using SEQUEST or MASCOT search algorithm and peak list generation in Thermo Proteome Discoverer 1.3.0.339 software (Thermo Fisher Scientific, USA). ThermoXcalibur Qual Browser was used as the search engine with Uniprot-rat.fasta (Database: Uniprot; Species: *Rattus norvegicus* (Rat); Taxon identifier: 10116; as accessed on 14-15/03/2018) as the sequence database. Following the search parameters like mass tolerance for precursor and fragment ion at 10 ppm and 0.1 Da, respectively, were selected for the analysis. Enzyme specificity was set to trypsin with less than two missed cleavage sites, static modification (peptide N-terminus) with iTRAQ 8 plex/+304.205 Da (K); methylthio/45.988 Da (C), dynamic modification with +15.995 Da (M) (oxidation). All identifications were filtered using the peak integration window tolerance of 20 ppm and analysis of the top 10 peaks. Estimation of the false discovery rate (FDR) was calculated using the parameter of target FDR as 0.01 at the peptide level. Proteins with at least two peptides were uniquely assigned to the respective sequence and were considered for further analysis at 95% significance level. All qualified proteins were exported to Microsoft Excel for manual data interpretation. Fold changes of proteins were presented in logarithmic scale and proteins with ≥1.5-fold difference (log₂ fold change ≥ ±0.585) and *p* ≤ 0.05 were considered as important deregulated proteins and selected for further analysis. A minimum set of selected proteins as important molecular signatures were selected for validation using Western blot assay and monitored in the treated subjects.

2.7 Western Blot

Equal amount of rat joint protein extracts (20 µg), from the animals not used in the discovery set, were subjected to electrophoresis on 12% sodium dodecyl sulfate polyacrylamide gel electrophoresis (SDS-PAGE). Separated proteins were transferred to PVDF membrane (Amersham Biosciences, UK) at 55 mA for 1.5 h in 25 mM Tris, 192 mM glycine, and 20% methanol using a TE 77-semidry transfer unit (GE Healthcare Biosciences, USA). Bovine serum albumin (BSA, 1% in Tris-buffered saline with 0.1% Tween-20 detergent: TBST) was used for blocking the nonspecific binding sites at 4°C by gentle shaking overnight. After washing with TBST buffer, protein transferred PVDF membranes were probed with respective primary antibodies (at 1:1000 dilution in TBST containing 0.25% BSA) against rat desmin (sc-23879, Santa Cruz, USA), vimentin (sc-32322, Santa Cruz, USA), T-kininogen (sc-103886, Santa Cruz, USA), alpha-1-antitrypsin (ab166610, Abcam, UK), nucleophosmin(ab10530, Abcam, UK), and GAPDH (sc365062, Santa Cruz, USA) for 3 h at room temperature. After washing, the blots were incubated with anti-rabbit (sc-2357, Santa Cruz, USA) or anti-goat IgG secondary antibodies (sc-2354, Santa Cruz, USA) conjugated with horseradish peroxidase (1:5000 in TBST containing 0.25% BSA) at room temperature for 2 h. The blots were washed again, equal volumes of solution A and B luminol reagents (sc-2048, Santa Cruz, USA) were properly mixed before adding to the blot and the resulting chemiluminescent signal was captured on an X-ray film (Kodak, India) in a dark room. Western blots were scanned using Image Scan and Analysis System (Alpha-Innotech Corporation, USA) (Bishwal et al., 2019). The band intensities were calculated using ImageJ and taken for densitometric analysis.

2.8 Protein-Protein Interaction Network Construction

The set of identified joint homogenate proteins from iTRAQ experiment was used to construct a protein-protein interaction (PPI) network using Cytoscape 3.6.0 (Shannon et al., 2003) appsGeneMANIA (Warde-Farley et al., 2010). Only the physical interaction network of arthritis-related genes was extracted from the constructed PPI. The network was curated after the deletion of the isolated node(s). So, a total of 434 nodes and 13,316 edges were built as a primary network graph and denoted by $G(N,E)$, where N represents the set of nodes with $N = \{ni\}; i = 1, 2, \dots, N$ while E denotes the set of edges with $E = \{eij\}; i, j = 1, 2, 3, \dots, N$.

2.9 Detection of the Levels of Organization

The communities of arthritic PPI networks were extracted using the community finding method of Newman and Girvan which is the first level of network organization (Blondel et al., 2008). It was established because of community interaction from the primary PPI network. The second organizational level was constituted by the subcommunities prepared from all communities forming the first level organization. Similarly, the succeeding levels were formed with the construction of *motifs*. Thus, each smaller community possesses at least one triangular *motif* as defined

by sub-graphG (Crofford, 2013; Crofford, 2013). *Motif G(3,3)* was used as the criteria of qualification for the community or sub-community as a constituting member at a certain level of organization because the triangular *motif* was overrepresented in the PPI network and served as the controlling unit in the network (Yeager-Lotem et al., 2004). Thus, each community belongs to different levels of the organization.

2.10 Topological Analyses of the Networks

The topological properties of the network for centralities, clustering coefficients, degree distribution, and neighborhood connectivity were analyzed by using Cytoscape plugins, NetworkAnalyzer (Assenov et al., 2008) and CytoNCA (Tang et al., 2015).

2.10.1 Degree (k)

In the process of network analysis, the total number of links is established by a node in the network and indicated by the degree k . This is also used to measure the local significance of a node in the network regulation process. In the graph represented by $G = (N, E)$, N denotes the nodes, while the edges are denoted by E . The degree of the i^{th} node (k_i) is expressed as $k_i = \sum_{ij}^N A_{ij}$, where the adjacency matrix elements of the graph is denoted by A_{ij} .

2.10.2 Probability of Degree Distribution ($P(k)$)

$P(k)$ denotes the probability of a random node for having a degree k out of the total number of nodes present in the network. This is represented as the fraction of nodes with degree (k), as presented in Eq. 2; here, N_k denotes the number of nodes to have degree k and N represents the total number of nodes in the network.

$$P(k) = \frac{N_k}{N} \quad (2)$$

$P(k)$ of small world and random networks always follow Poisson's distribution in a degree distribution against degree (k), however most of the real-world networks which are hierarchical and scale-free follow the power law distribution $P(k) \sim k^{-\alpha}$ and 4.2. In the hierarchical networks, ~ 2.26 (mean-field value) indicates a hierarchical modular organization at different topological levels (Ravasz and Barabási, 2003). Thus, the characteristic topology of a network is defined by $P(k)$ pattern.

2.10.3 Clustering Coefficients $C(k)$

It is the ratio of the number of triangular motifs created by a node with its nearest neighbors and the total number of such motifs in the entire network. Therefore, $C(k)$ characterizes the strength of internal connectivity within the node neighborhoods quantifying the inherent clustering tendencies of nodes. Eq. 3 expresses $C(k)$ for any node i with the degree k_i in a unidirectional graph. In this equation, m_i represents the total number of edges among its nearest neighbors. In the scale-free networks $C(k) \sim \text{constant}$, however it shows the power law in a hierarchical network against the degree, $C(k) \sim k^{-\alpha}$, with $\alpha > 1$ (Ravasz and Barabási, 2003).

$$C(k) = \frac{2m_i}{k_i(k_i - 1)} \quad (3)$$

2.10.4 Neighborhood Connectivity $C_N(k)$

The node neighborhood connectivity is the average connectivity which is established by the nearest-neighbors of a node with degree k . It is represented by $C_N(k)$ as shown in Eq. 4, where $P(q|k)$ is a conditional probability of a node's links with k connections to one of the other nodes having q connections.

$$C_N(k) = \sum_q qP(q|k) \quad (4)$$

In the hierarchical network topology, $C_N(k)$ shows power-law against the degree k , i.e., $C_N(k) \sim k^\beta$, here $\beta \sim 0.5$ (Pastor-Satorras et al., 2001). The negativity or positivity of the exponent β may be defined as the disassortative or assortative nature of network topology, respectively (Barrat et al., 2004).

2.10.5 Centrality Measures

Betweenness centrality C_B , closeness centrality C_C , Eigenvector centrality C_E are the basic centrality measures and are the parameters for the estimation for a node's global functional significance in a network regulation through information processing (Newman and Girvan, 2004).

The total geodesic distance between a node and all its connected nodes is given by C_C . It also determines how rapidly information is spread within a network from one node to other connected nodes (Canright and Engø-Monsen, 2004). In each network, C_C of a node i is calculated by dividing the total number of nodes of network n by the summation of geodesic path lengths between the nodes i and j which is given by d_{ij} in Eq. 5.

$$C_C(k) = \frac{n}{\sum_j d_{ij}} \quad (5)$$

The C_B or betweenness centrality is the measure of a node which is a share of all the shortest-path traffic from all feasible routes through nodes i to j . So, it is the parameter of the ability of a node to extract benefit from the flow of information throughout the network (Brandes, 2001) and its ability to control the signal processing over the other nodes within the network (Estrada and Rodríguez-Velázquez, 2005). If $d_{ij}(v)$ represents the number of geodesic paths from one node i to another node j passing through node v , then $C_B(v)$ of node v can be derived from Equation 6.

$$C_b(v) = \sum_{i,j:i \neq j \neq k} \frac{d_{ij}(v)}{d_{ij}} \quad (6)$$

The normalized betweenness centrality is summarized in Eq. 7, in which M represents the number of node pairs, excluding v .

$$C_B(v) = \frac{1}{MC_b(v)} \quad (7)$$

Eigenvector centrality C_E corresponds to the intensity of the most prominent nodes affecting signal processing throughout the network and is proportional to the sum of the centralities of all neighbors of a node (Canright and Engø-Monsen, 2006). In a network, the nearest neighbors of node i is given by $m(i)$ with eigenvalue and the eigenvector v_i of

eigen-value equations, $Av_i = v_i(\lambda)$ where, A is the network adjacency matrix, C_E can be calculated by Eq. 8,

$$C_E(i) = \frac{1}{\lambda} \sum_{j \in m(i)} v_j \quad (8)$$

The value of C_E gives the maximum positive eigenvalue, λ_{max} of the principal eigenvector of A (Canright and Engø-Monsen, 2006). A node's C_E function is dependent on the centralities of its neighbors, and it varies according to different network association of high C_E nodes. There are lesser chances of isolation of nodes within the closely connected regions of such nodes (Canright and Engø-Monsen, 2006). Thus, C_E is considered as an influential indicator of the information transmission power of a node within a network.

2.11 Tracking the Key Regulators in the Networks

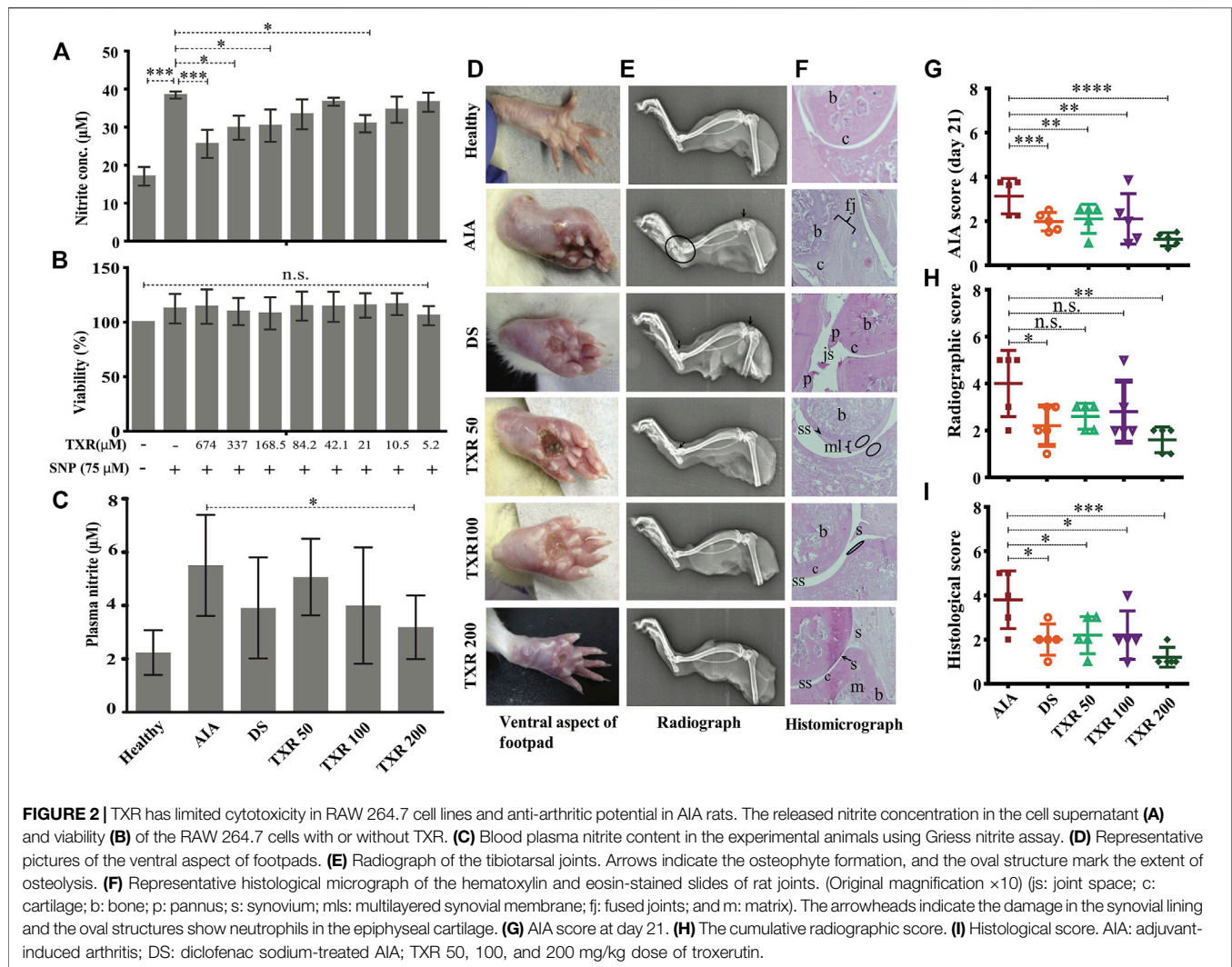
The most prominent genes or the corresponding proteins of the arthritic network were first identified by the centrality measures calculation. As the higher degree nodes possess higher centrality values, we considered the top 65 highest degree nodes ($degree\ k \geq 65$) among the hub nodes to trace the key regulators which may have a very important role to play in the network regulation. Then the nodes were traced from the primary network up to the motif levelG (Crofford, 2013; Crofford, 2013). This tracing was performed based on the representation of respective nodes (proteins) throughout the submodules obtained from the community clustering method of Louvain. Therefore, the key regulators of the arthritic network were the hub-nodes (proteins) which corresponded to the modules at all the hierarchical levels in the arthritic network.

2.12 Molecular Docking Study

The identified key regulators were studied for their molecular interaction with troxeerutin. The structures of the proteins were either taken from the Protein Data Bank (PDB) or the primary sequence of key regulators is retrieved from NCBI for homology modeling. iTASSER servers were instrumental for homology modeling of the key regulator proteins (Yang et al., 2014). The docking study is performed using AutoDock vina, Discovery Studio, Schrödinger Glide software, and the interactions were visualized with PyMOL (DeLano, 2014), Chimera (Goddard et al., 2007), Discovery Studio Visualization (Accelrys, San Diego, CA, United States), and Maestro (Repasky et al., 2007).

2.13 Statistical Analysis

All the samples (cell and animals) were randomly selected for each experimental group. Based on our experience, the sample and animal sizes were selected to achieve sufficient statistical power to identify relevant differences, if any. Based on the distribution of the data and the number of study groups used for comparative analysis, appropriate statistical tests were explored for determining the levels of significance. Two-way analysis of variance (ANOVA) with Bonferroni post-test corrections for multiple comparisons with uncorrected Fisher's LSD test were used for determining the difference between AIA



and other groups, for AIA score, arthritic index, change in footpad thickness, and body weight. Whereas one-way ANOVA with Dunnett's post-tests for multiple comparisons was used for a radiographic score, all the histological scores, Griess assay in cell culture, MTT assays, and Western blot results. The student's *t*-test was used to determine levels of significance between the groups in the iTRAQ proteomics studies. All these statistical tests were performed using GraphPad Prism7. Results are presented as the mean \pm SD; statistical significance is indicated as follows: * $p \leq 0.05$; ** $p \leq 0.01$; *** $p \leq 0.001$.

3 RESULTS

3.1 TXR Inhibits SNP Stimulated Nitrite in Cell Culture Without Cytotoxicity

RAW264.7 cells (10^5 cells/ml) treated with TXR (674 μ M) showed similar nitrite levels with SNP stimulated controls ($p < 0.0001$) (Figure 2A). With lower TXR levels, nitrite concentration showed an increase in trend from 25.6 μ M in the highest

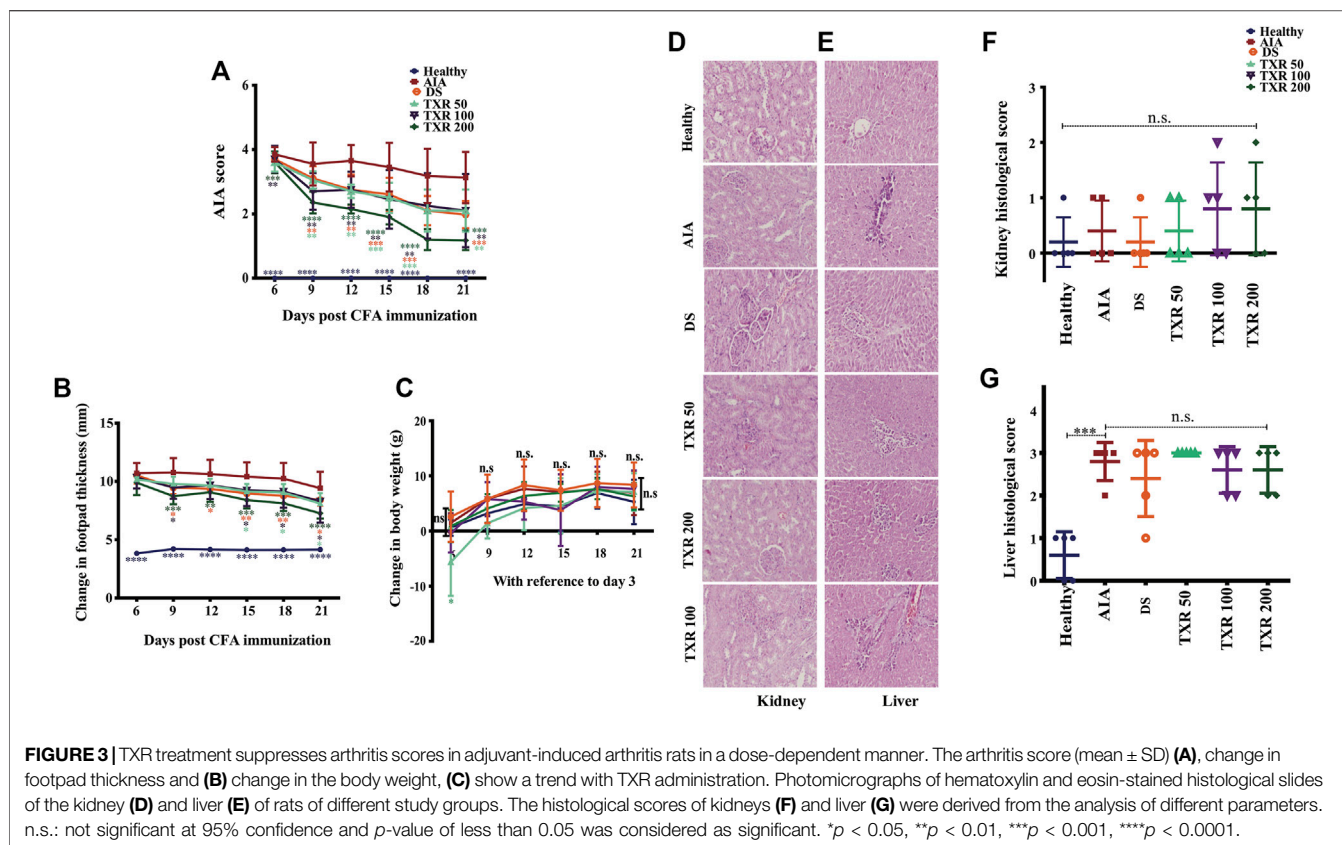
concentration to 29.8 μ M ($p < 0.05$) in 337 μ M TXR, 30.4 μ M in 168.5 μ M ($p < 0.05$). Cells treated with SNP and TXR at varying concentrations (674–5.26 μ M) showed similar viability (Figure 2B).

3.2 Effect of TXR on Plasma Nitrite Concentration

In the AIA group, a higher (2.5-fold) plasma nitrite level was observed with respect to healthy animals. In TXR-treated groups, lower plasma nitrite levels were observed in a dose-dependent manner (8.02% in TXR50, 27.49% in TXR100, and 42.24% in TXR200) with respect to the AIA group. In the TXR200 group, the lowest nitrite levels were observed in the plasma of AIA animals ($p < 0.05$). TXR100 and DS showed a similar effect (~29.06% decrease) on plasma nitrite levels as depicted in Figure 2C.

3.2.1 Joint Radiographic and Histopathology Analyses Show Protective Effects of TXR

The footpad thickness at the disease onset was the highest and resolved during the treatment (Figure 2D). The limb

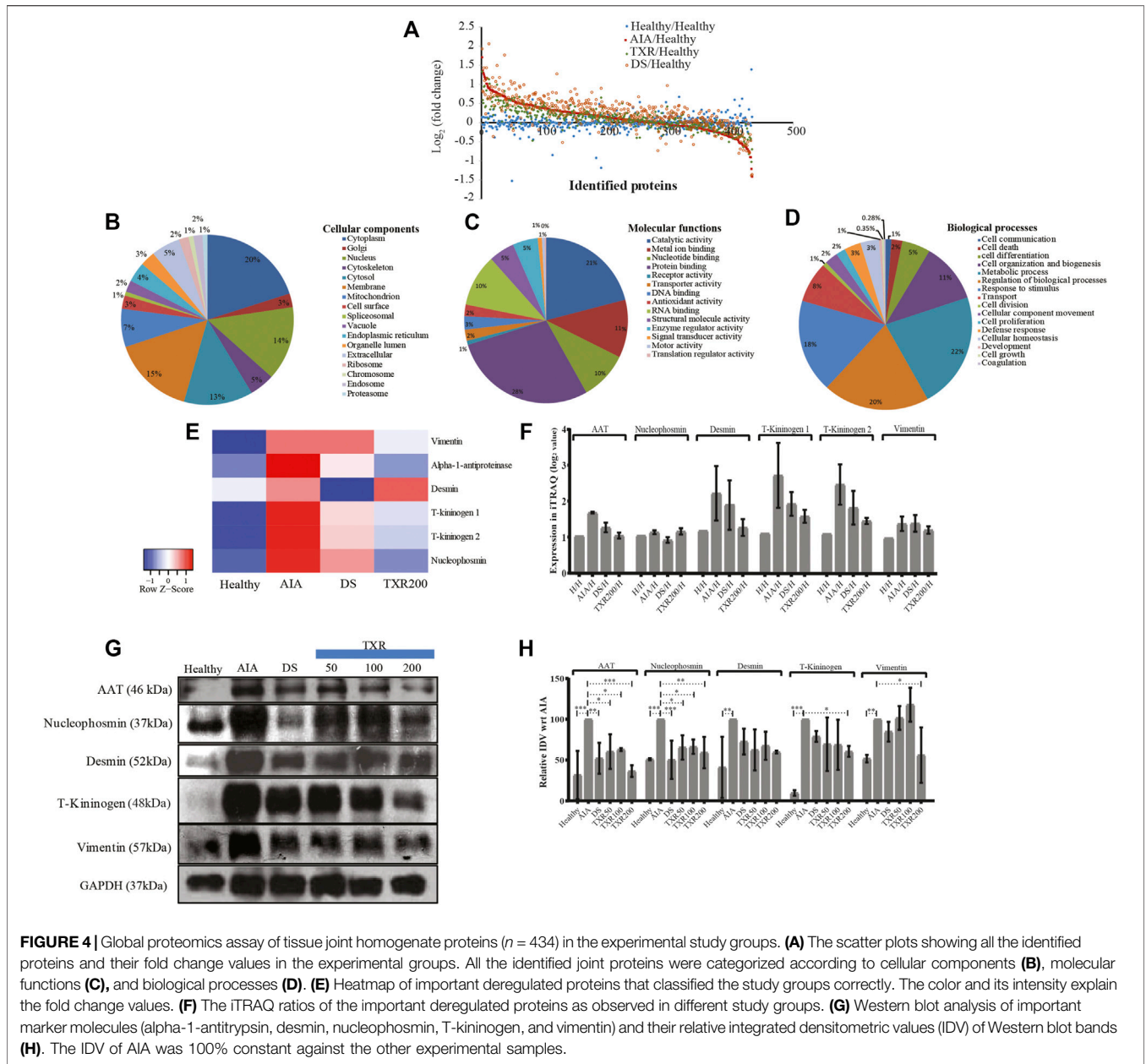


roentgenograms of the experimental animals showed joint erosion with osteophyte formation; edema and soft tissue with noticeable swelling (Figure 2E). The AIA group showed considerable damage with bone erosion and reduction in the joint space. In TXR200 ($p \leq 0.01$) and DS ($p \leq 0.05$) groups, a significant recuperation of the joint damage was observed. The AIA group exhibited drastic inflammation of the tibiotarsal joints resulting in an increase in the thickness of the bones and cartilages (Figures 2E,F). All the treatment groups showed a reduction in osteological swelling in the tibiotarsal joints. The tibiofemoral joints were less affected as compared to tibiotarsal joints in all the groups. However, AIA and DS groups exhibited signs of damage (Figures 2E,F). AIA score at day 21 showed a significant reduction in the TXR200 group (Figure 2G). There was a marked reduction in the radiographic scores of TXR50 and TXR100 but were not statistically significant (Figure 2H). In the plantar regions, reduced soft tissue swellings were observed in the TXR-treated groups. The histopathological data of all the groups was expressed in terms of the histological score (Figure 2I).

3.2.2 TXR Treatment Suppresses Disease Progression in Arthritis

The arthritic symptoms appeared within 18–36 h of adjuvant immunization and the inflammatory parameters were edema, periarticular erythema, and functional decline in the gait of the

immunized rats (Figure 3). The gait of the arthritic animals improved substantially in all the TXR-treated groups as compared to the AIA group, which was included as a parameter in the arthritic score calculation throughout the treatment period (Figure 3A) and on the day of sacrifice, i.e., day 21 (Figure 2G). TXR (200 mg/kg) treatment has brought down the arthritis score close to the basal level (healthy) (Figure 3A) and showed a visible effect in the hind footpads of the rats (dorsal view, Figure 1C, and ventral view, Figure 2D). A significant reduction of the mean arthritic score was observed in a dose-dependent manner from day 6 (dorsal view, Figure 1C, and ventral view, Figure 2D). AIA score pattern was found to be similar in TXR100 and DS groups, whereas in TXR50, positive effect was observed by day 12. Arthritis ameliorating potential of TXR at 50 and 100 mg/kg was found to be comparable to DS treatment based on the appearance of secondary lesions in the footpad and tail base. A marked decline in AIA score in TXR200 from day 6 ($p \geq 0.05$) till day 21 ($p \leq 0.0001$) was observed (Figure 3A). Dose-dependent remissions of lesions in the subplantar region were observed in the TXR-treated groups. The TXR200 group showed rapid wound healing and erythema with respect to TXR100, TXR50, and DS groups. AIA score, on the experiment termination day (day 21), showed highly significant improvement ($p < 0.0001$) in TXR200 followed by DS ($p = 0.0006$) and TXR100 and TXR50 groups (both $p = 0.002$).



3.2.3 Reduction in Footpad Thickness Upon TXR Treatment

Significant reduction of mean footpad thickness in TXR-treated groups was observed in a dose-dependent manner (Figure 3B). In TXR200, a continuous reduction in swelling as compared to the AIA group from day 9 till day 21 was observed. TXR100 and DS exhibited a similar trend throughout the experimental period, while TXR50 showed the least inhibitory effect.

3.3 TXR has a Minimal Adverse Effect in the Treatment of Arthritis

3.3.1 Effect of TXR on Body Weight Gain

All experimental animals showed normal weight gain during the experimental period. The AIA and healthy animal groups showed

similar weight gain till day 21. Body weight gain in the TXR50 group followed a different trend than the other experimental groups (Figure 3C). TXR100 and TXR200 groups showed insignificant weight change with respect to the AIA or healthy groups. This can be attributed to the beneficial effects of TXR overcoming its adverse effects due to the lower dose.

3.3.2 Effect of TXR on Liver and Kidney Histology

We observed the absence of liver steatosis, sinusoidal dilatation, Kupffer cell hyperplasia, apoptosis, and necrosis in the liver tissues of TXR-treated animals (Figures 3D,E). The presence of eosinophils in the portal tracts and sinusoids suggested drug-induced liver injury (DILI). The TXR-treated groups showed insignificant differences in the liver and kidney histological scores when compared to the AIA group (Figures 3F,G). Based on the

liver histological score, AIA induction contributes to liver damage (Figures 3E,G). With the administration of DS or TXR, the liver histological score remains at par with the AIA group. At any given dose, TXR did not improve AIA-induced liver or kidney damage ($p > 0.05$) when compared to AIA.

3.4 Effect of AIA and TXR Treatment on Joint Homogenate Proteome

A total of 434 joint proteins were identified in the experimental groups (Figure 4A; Supplementary Table S1). A positive correlation was observed in the biological replicates of AIA ($R^2 = 0.569$), TXR ($R^2 = 0.597$), and DS ($R^2 = 0.512$) groups (Supplementary Figures S2A–S2C). A set of 65 proteins showed deregulation (fold change ≥ 1.5) in AIA with respect to the healthy group (Supplementary Figure S2A). 49 (Noris and Remuzzi, 2013) proteins out of 65 were found upregulated, while 16 were downregulated in the AIA group with respect to healthy controls (Supplementary Table S2). When compared with AIA, in TXR-treated groups, 11 (9 \uparrow and 2 \downarrow) proteins with ≥ 1.5 -fold change was upregulated (Supplementary Table S3), while 27 proteins were found to be significantly ($p \leq 0.05$) deregulated (Supplementary Table S4). When the DS group was compared with AIA, 19 (7 \uparrow and 12 \downarrow) proteins were ≥ 1.5 fold deregulated, and 17 proteins were significantly deregulated. Three proteins (complement component 9, C-reactive protein, and α -1, β -glycoprotein) were found to be significantly differentially expressed and are known as inflammatory mediators playing critical roles in arthritis pathogenesis (Supplementary Figure S3A). Two important inflammatory mediator proteins (C-reactive protein and adenylate-kinase isoenzyme-1) showed deregulation in the DS group (Supplementary Figure S3A). A set of 5 proteins (AAT, T-kininogen, vimentin, nucleophosmin, and desmin) were sufficient to classify the AIA diseased groups from the healthy group and were selected for further validation. We have also compared the differential expression of proteins in TXR, and DS-treated groups with the healthy animals to find that 28 ($\uparrow 24$ and $\downarrow 4$) proteins in TXR (vs. healthy group) (Supplementary Table S5), while 87 ($\uparrow 76$ and $\downarrow 11$) proteins in DS (vs. healthy group) with ≥ 1.5 -fold change.

3.5 Functional Categorization of the iTRAQ Identified Proteins

The identified proteins from the iTRAQ experiment were functionally annotated according to the cellular location, molecular function, and biological processes (Figures 4B–D). Most of these proteins were of cytoplasm (20%), membranous (15.4%), nucleus (14.9%), cytosolic (12.9%), and mitochondrial (7.25%) origin (Figure 4B). On the other hand, the identified proteins are involved in more than one molecular function and found to possess protein binding (28.4%), catalytic activity (20.9%), metal ion activity (11.3%), RNA binding (10.2%), and nucleotide activity (9.5%) (Figure 4C). It was observed that in biological processes, 22% of these proteins are primarily involved in metabolic processes, 20% represent regulation of biological processes, 18% proteins are expressed in response to stimuli, 11%

are involved in cell organization and biogenesis, 8% are transport proteins, 5% are involved in cell differentiation, while the remaining 16% proteins play other important roles (Figure 4D).

3.6 Relative Expression of Proteins in iTRAQ and Western Blot Experiment

The fold change values of identified important sets of proteins from the iTRAQ experiments (Figures 4E,F) were monitored in independent samples using Western blot analysis (Figures 4G,H; Supplementary Figure S3B). For example, T-kininogen, a rodent-specific inflammatory mediator, increased (~ 15.4 fold) with arthritis induction and significantly reduced in TXR200 to 2.8-fold. DS, TXR100, and TXR50 groups showed similar levels of T-kininogen as observed in the AIA group. An abundance of both, T-kininogen-1 and T-kininogen-2, were found to be similar in mass spectrometry and in the Western blot data. TXR200 treatment reduced both T-kininogen-1 and T-kininogen-2 levels as observed in iTRAQ analysis. Marked reduction in vimentin level was evident in TXR200 treatment, whereas TXR50, TXR100, and DS did not show considerable change in vimentin as compared to AIA. A higher abundance of AAT was observed in AIA compared to the healthy ones and with DS treatment, the expression was reduced. The level of AAT showed a reduction with TXR treatment in a dose-dependent way. A similar trend was observed in desmin and nucleophosmin levels. With respect to the AIA group, a lower nucleophosmin level was observed in the DS-treated group.

3.7 The Arthritic PPI Network Follows Hierarchical Scale-Free Topology Composed of the Modules at Different Levels of Hierarchy

From the primary network of the identified proteins was constructed, using the interactome network of 434 proteins, the physical interacting PPI network of 434 proteins with 434 nodes and 13,316 edges (Figure 5A). This primary arthritic network upon analysis showed that power-law distributions for the probability of node degree distribution, $P(k)$, clustering coefficient $C(k)$ with negative exponents, and neighborhood connectivity distribution $C_N(k)$ against degree (k) with positive exponents were followed (Eq. 9) (Figure 5B) (Pastor-Satorras et al., 2001). This power-law feature shows that the network exhibited hierarchical-scale free behavior with the system-level organization of communities. Detection of the sub-communities and communities at different levels of organization was possible with the use of the Louvain modularity optimization method (Blondel et al., 2008) as shown in Figure 5C. The arthritic network has six hierarchical levels of the organization. As a result, 122 communities and smaller communities were found, and 6 of them could reach up to the bottom motif level.

Communities at the first hierarchical level exhibited the power-law distribution for $P(k)$ and $C(k)$ against degree distribution with negative exponents further demonstrating system-level organization of the modules (Equation 9). $C_N(k)$ exhibits the power-law against degree k with a positive exponent

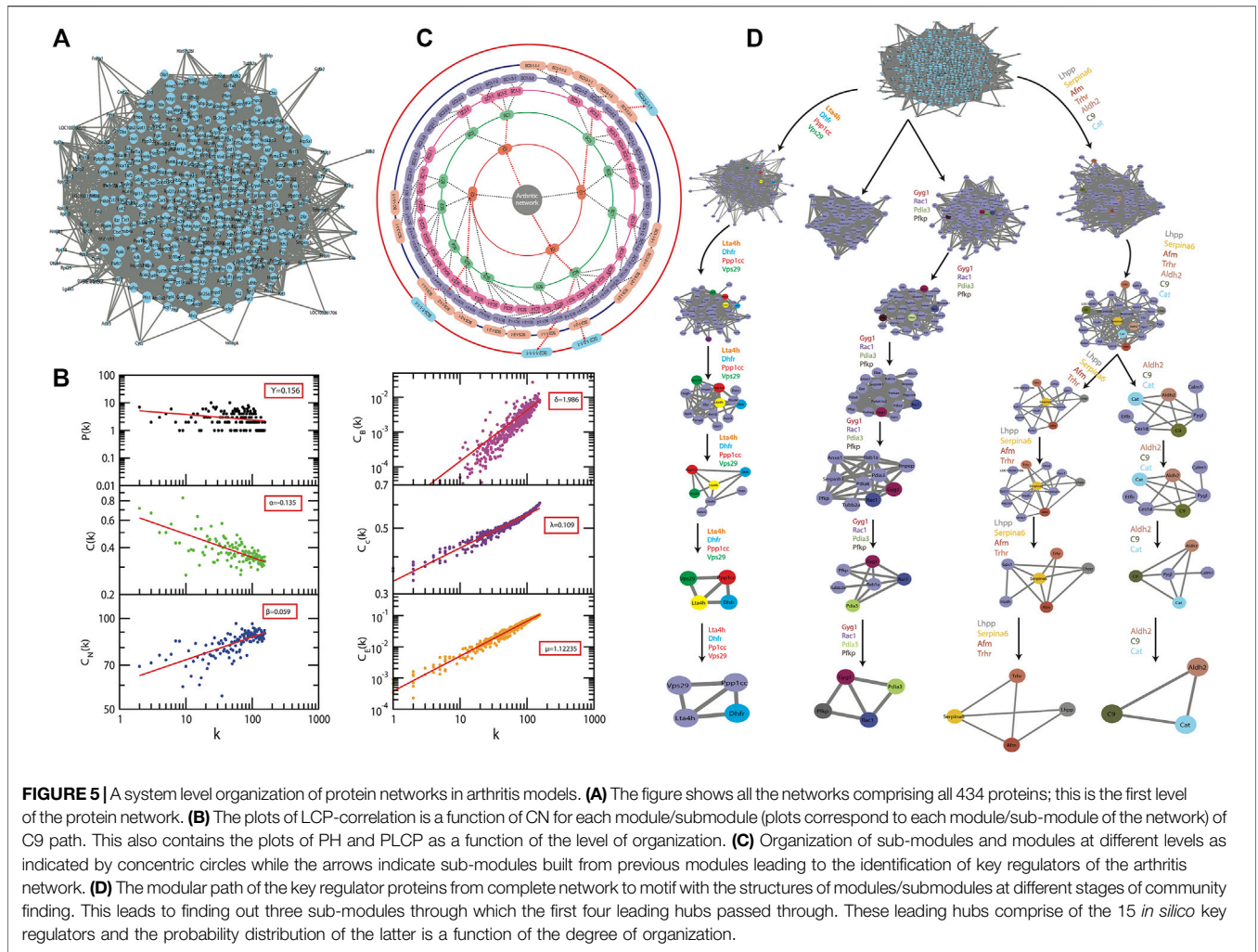


FIGURE 5 | A system level organization of protein networks in arthritis models. **(A)** The figure shows all the networks comprising all 434 proteins; this is the first level of the protein network. **(B)** The plots of LCP-correlation is a function of CN for each module/submodule (plots correspond to each module/sub-module of the network) of C9 path. This also contains the plots of PH and PLCP as a function of the level of organization. **(C)** Organization of sub-modules and modules at different levels as indicated by concentric circles while the arrows indicate sub-modules built from previous modules leading to the identification of key regulators of the arthritis network. **(D)** The modular path of the key regulator proteins from complete network to motifs with the structures of modules/submodules at different stages of community finding. This leads to finding out three sub-modules through which the first four leading hubs passed through. These leading hubs comprise of the 15 *in silico* key regulators and the probability distribution of the latter is a function of the degree of organization.

($\beta \sim 0.05, 0.13$ and 0.14 , respectively) (**Figure 5D**). This specifies the assortative nature of the modules reflecting the possibility of the formation of rich-club and the hubs play a very important role in the maintenance of network stability and properties (Pastor-Satorras et al., 2001).

$$\begin{aligned}
 (P(k)C(k)C_N(k)) &\sim (k^{-\gamma}k^{-\alpha}k^{-\beta}); (\gamma \alpha \beta) \\
 &\rightarrow (0.82 - 2.520.15 - 0.670.02 - 0.57)
 \end{aligned}
 \tag{9}$$

3.8 The Fifteen (15) Novel Key Regulators of the Network Are Its Backbone

There is a very important role of the nodes in the information processing within a network and this is well assessed by the centrality measures such as the C_B , C_C , and C_E . These are the different topological properties that determine the signal transmission efficiency of a network (Estrada and Rodríguez-Velázquez, 2005). In the network and modules of arthritis, at first hierarchical level, these factors also demonstrated power-law as the function of degree (k) with positive exponents, with an increase in the degree of nodes the centralities tend to get

increased (**Eq. 10**) (**Figure 5B**). The values of the exponents of C_B , C_C , and C_E for the first level of network organization are found to be $\delta = 1.986$, $\lambda = 0.109$, and $\mu = 1.12235$.

$$\begin{aligned}
 (C_B(k)C_C(k)C_E(k)) &\sim (k^\delta k^\lambda k^\mu); (\delta \lambda \mu) \\
 &\rightarrow (1.745 - 2.0120.091 - 0.1721.102 - 1.321)
 \end{aligned}
 \tag{10}$$

Thus, there is an increase in the signal processing efficiency with the higher degree nodes emphasizing the significant roles of these nodes in the flow of information, regulation, and stabilization of the network. Therefore, the *hub* proteins must have played a significantly large influence in the network regulation and pathogenesis of arthritis. The 122 modules of proteins were taken into consideration to find out the most important proteins as they were present at each topological level resulting in the identification of the most high-ranking key regulator proteins in the arthritic network. After tracing *hubs* at every topological level, 15 (Tarantino et al., 2009) proteins (*C9*, *Aldh2*, *Pdia3*, *Serpina6*, *Afm*, *Gyg1*, *Ppp1cc*, *Pfkfb*, *Dhfr*, *Cat*, *Trhr*, *Vps29*, *Lta4h*, *Rac1*, and *Lhpp*) (**Supplementary Table S6**) were established as the backbone of the entire network. The key regulators which form the *motifs* with their partners

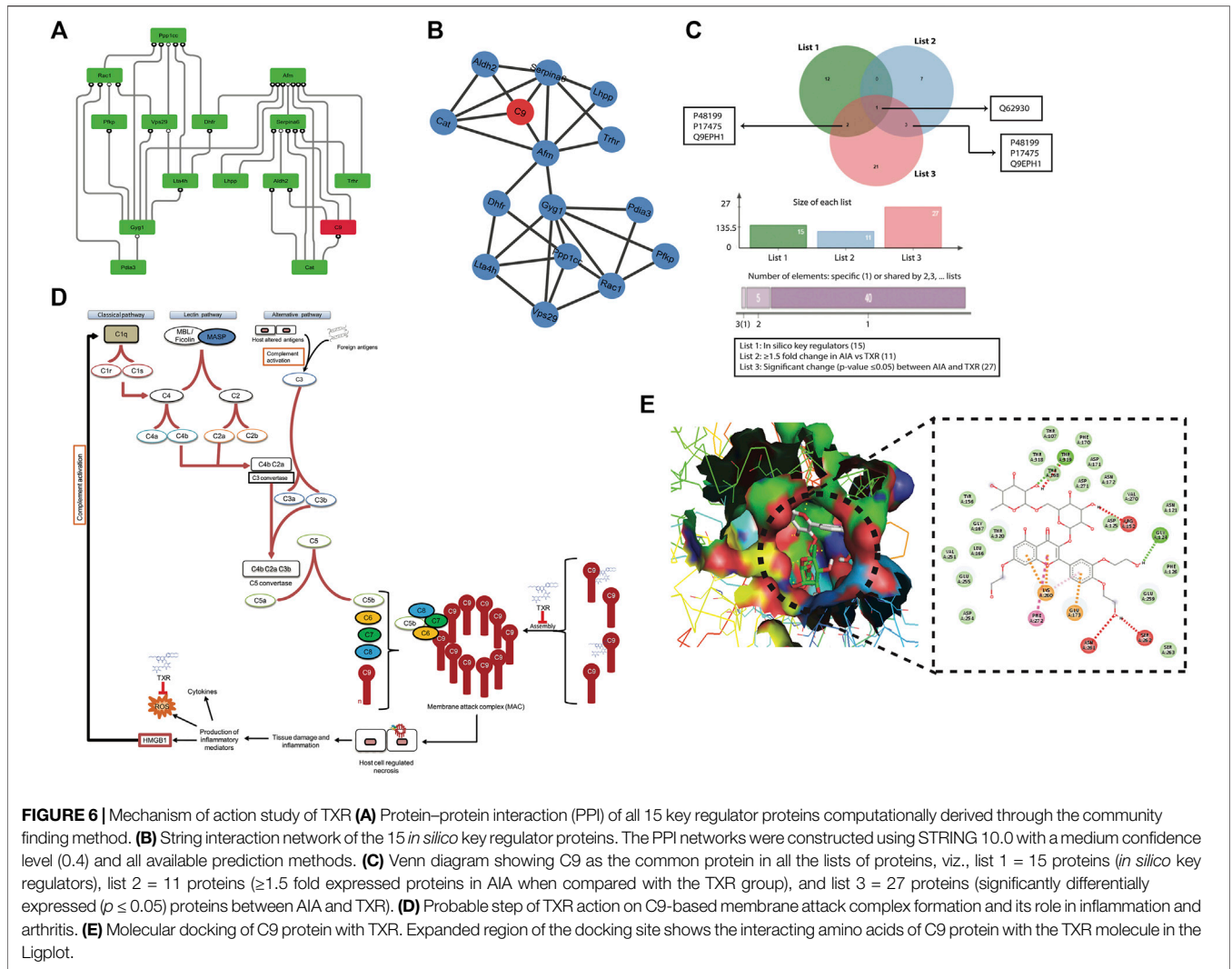


(Figure 5D) might be instrumental in the network integrity, optimization of signal processing, dynamics, maintaining the stability, and most importantly, regulation of the network. Our community finding method confirmed that all 15 key regulators are interacting with each other (Figure 6A). This PPI was later validated using the database of STRING 10.0 (Figure 6B).

3.9 C9 as the Most Common Protein in Different Groups

We found four proteins (C9, protein disulphide isomerase A3, thyrotropin-releasing hormone receptor, and isoform gamma-2 of serine/threonine–protein phosphatase 1) as common from the list of *in silico* key regulators ($n = 15$) and the list of ≥ 1.5 -fold changed proteins in AIA vs. healthy ($n = 65$) (Supplementary Figure S4A). Whereas 2 proteins (adenylate kinase isoenzyme 1 and C-reactive protein) were found to be common when the list of ≥ 1.5 -fold changed proteins in AIA vs. DS ($n = 19$) and the list of significantly ($p \leq 0.05$) deregulated proteins in AIA vs. DS ($n = 17$) were matched (Supplementary Figure S4B). The Venn

diagram presents the common list of proteins from *in silico* key regulator proteins ($n = 15$), ≥ 1.5 -fold changed proteins in AIA vs. healthy ($n = 65$), ≥ 1.5 -fold changed proteins in AIA vs. TXR ($n = 11$), and significantly changed proteins between AIA vs. TXR ($n = 27$) (Supplementary Figure S4C). C9 was identified as the most common protein from these 4 lists. This signifies the importance of C9 as the molecular target of TXR. No common protein was found in the Venn diagram of the five lists together (excluding the $n = 65$ list) (Supplementary Figure S4D).

3.10 Molecular Interaction of Key Regulators With TXR Through *In Silico* Docking

The combination of these distinct methods, viz., iTRAQ differential proteomics and *in silico* network analysis studies, helped narrow down our search to the very specific protein with the probability of being the target of TXR, i.e., the complement component 9 (C9) (Figure 6C). The role of C9 is critical for the formation of membrane attack complex (MAC) resulting in tissue

injury which further activates the entire complement pathway (Figure 6D). All these compounds were found positioned in the deep cavity of the proteins which show several close interactions to their catalytic residues (Supplementary Figure S5) along with C9 (Figure 6E). Here, several residues of the binding pocket have formed strong hydrogen bonds with the compound TXR in addition to several Van der Waals and other weak interactions to properly hold it in the binding cavity of the proteins. Thus, we proposed TXR as a potential scaffold that can be used in the development of potential inhibitors of this protein.

Molecular docking studies with C9 showed highest binding affinity (-8.9 kcal/mol) of TXR with the interacting residues of THR168, THR319, ARG152, GLY124, SER262, ASN261, GLU173, LYS260, and PHE272 (Figure 6E; Supplementary Table S6) followed by other 14 key regulators Aldh2 (-7.3 kcal/mol), Pdia3 (-8.0 kcal/mol), Serpina6 (-5.9 kcal/mol), Afm (-7.9 kcal/mol), Gyg1 (-6.7 kcal/mol), Ppp1cc (-6.7 kcal/mol), Pfkp (-7.3 kcal/mol), Dhfr (-7.5 kcal/mol), Cat (-7.1 kcal/mol), Trhr (-6.6 kcal/mol), Vps29 (-7.2 kcal/mol), Lta4h (-8.5 kcal/mol), Rac1 (-6.3 kcal/mol), and Lhpp (-6.4 kcal/mol) (Supplementary Table S6; Supplementary Figure S5). Proteins associated with the inflammatory processes such as acute-phase plasma proteins or others may indicate intervention by TXR in the disease progression. Therefore, investigating the effect of therapeutic compounds on the expression of plasma proteins in arthritic rats was of importance in our earlier study also (Sahu et al., 2012). We used the network theoretical approach which has considered the hubs, motifs, and modules of the network with equal emphasis for the identification of key regulators or the significant regulatory pathways preventing any bias toward the overrepresented hubs or motifs. A relationship between hubs, motifs, and modules was established and the network used all the proteins associated with the disease instead of the merely manually curated dataset usage. In conclusion, the hubs with the highest degree were identified, 15 (Tarantino et al., 2009) were considered as the novel key regulators.

4 DISCUSSION

The autoimmune disease, RA is an incurable and difficult to manage disease. Identification of pharmacological compounds with minimum side effects is a way forward for its management. The current pharmaceutical solutions involve disease-modifying arthritis drugs which work in ~60% of the cases, and in certain populations can lead to adverse reactions like pneumonia, tuberculosis, and interstitial pneumonitis. Identification of predictive markers might facilitate the development of personalized therapy to gain optimum treatment benefit in RA patients. In this study, we monitored the antiarthritic potential of a phytochemical i.e., TXR, and investigated its probable mechanism of action by identifying its target proteins in the joint homogenate.

In our *in vitro* studies, TXR has significantly reduced the nitrite levels with negligible effects on cell viability up to a concentration of 674 μ M as shown by MTT assay. It is widely reported that TXR is a phytochemical with proven health benefits. It also has very low toxicity (LD₅₀ of 27160 mg/kg body weight in

rats) and is safe for human use (Zhang et al., 2015a; Zhang et al., 2015b; Shan et al., 2018; Li et al., 2019).

We used a commonly adopted AIA animal model and observed the manifestation of the RA disease parameters. With TXR treatment, there was a significant reduction of radiographic and histological scores in all the AIA study groups receiving treatment in a dose-dependent manner. A significant decrease in the footpad thickness was observed and similar body weight gain was noticed in the TXR-treated AIA groups. Based on the histological analyses of the liver and kidneys, it seems that the damage caused by AIA was not corrected with TXR or DS treatment. We used DS as a control drug and other antiarthritic drugs could be used for the comparative analysis in subsequent studies. A set of 65 proteins was found to be dysregulated in the joint homogenate of the AIA group as compared to the healthy group of which 11 proteins showed a positive correlation with TXR treatment. Many of these deregulated proteins participate in inflammation, arthritis, autoimmune disorders, and cancer. Upon TXR administration, many dysregulated proteins at the time of disease onset showed time-dependent reversal to the basal level. A set of 5 proteins (AAT, nucleophosmin, desmin, T-kininogen, and vimentin) were sufficient to classify the AIA diseased groups from the healthy group and were thus selected for Western blot validation. An abundance of these proteins was probed in the joint tissues of independent sample sets using Western blot experiments and corroborated the mass spectrometry findings.

The PPI study of the identified protein sets and the protein community finding by *in silico* network analysis identified a set of key regulator molecules (Ali et al., 2018; Farooqui et al., 2018; Malik et al., 2019; Mangangcha et al., 2019). The constructed primary PPI arthritis network tracked from the level of hubs up to the motifs resulted in the detection of key regulators (hubs) from a total of 434 identified proteins. Employing Newman and Girvan's method (Newman and Girvan, 2004) for community findings with equal importance to the modules, motifs, and hubs of the network, resulting in the identification of 15 novel key regulators (C9, Aldh2, Pdia3, Serpina6, Afm, Gyg1, Ppp1cc, Pfkp, Dhfr, Cat, Trhr, Vps29, Lta4h, Rac1, and Lhpp) which are the known markers involved in some other diseases also. In addition, these key regulators have other interacting partners at the level of motifs which may also have importance in arthritis pathogenic mechanisms, thus establishing them also as candidate disease regulators. Combining the mass spectrometry and *in silico* analysis, the complement component 9, C-reactive protein, catalase, aldehyde dehydrogenase, α -1-antiproteinase, and α -1B glycoprotein (AAG) were selected as the common key regulators.

Upon TXR treatment, the C9, AAG, and catalase abundance were decreased almost to the basal levels without significant alterations in CRP, a nonspecific indicator of inflammation. High aldehyde dehydrogenase (ALDH) activity has been reported in osteoarthritis patients' chondrocytes and elevation of Serpinal was also observed in the joint homogenates of the AIA group (Unguryte et al., 2016). ALDH and AAT are known to have tissue-protective properties in arthritis. AAT is an acute-phase protein, possessing immunoregulatory and anti-inflammatory functions independent of antiproteinase activity. In the collagen-induced

arthritis (CIA) model, a higher AAG level has been reported (Serada et al., 2010; Urushima et al., 2017). C9 is one of the multimeric components of the terminal stage of all the complement pathways, resulting in the MAC which initiates cellular lysis at the target tissue i.e., chondrocytes of the cartilage in the synovial joints. C9 may be responsible for the cartilage degradation leading to joint tissue damage in the autoimmune and reactive arthritis conditions. We have found that TXR disrupts the MAC mediated complement pathway (**Figure 6D**), however, further investigation at the biophysical level will be beneficial.

Activation of the entire complement cascade results in the formation of MAC which initiates proinflammatory responses causing autoimmune diseases (Noris and Remuzzi, 2013). Thus, TXR ameliorates arthritis by the inhibition of the complement-mediated autoimmune pathogenesis. There have been many successful attempts for the containment of the complement-mediated pathogenesis in arthritis by targeting various components of all three major complement pathways (Lappegård et al., 2015). Lappegård et al., described various inhibitors of the complement component pathway, however, to the best of our knowledge there has been no inhibitor or blocker reported for the C9 component of MAC. Through our present study, we proposed that TXR is a potent inhibitor of MAC, which is a complex of transmembrane proteins composed of C9 subunits. MAC is responsible for channel formation across the plasma membrane of the target cell resulting in its lysis. The channel thus formed allows the inflow of several ions (Ca^{2+} , Na^{+}) causing endosmosis followed by necrotic cytolysis, thus releasing the cytokines and other related inflammatory mediators into the milieu. Thus, it may promote the production of interleukin 1 beta ($\text{IL-1}\beta$) through Nod-like receptor protein 3 (NLRP3) inflammasome, thus acting as an immune-stimulating factor (Kelley et al., 2019). MAC-mediated necrosis of the target cells (chondrocytes, osteocytes, and synoviocytes) releases inflammatory mediators like cytokines, high-mobility group box 1 (HMGB1) resulting in further joint damage (García-Arnandis et al., 2010). The cytokines, in turn, stimulate other cells to activate the complement pathway (Markiewski and Lambris, 2007), thus aggravating the inflammatory response manifold. Extracellular HMGB1 binds to C1q, thus activating the classical complement pathway followed by the reformation of MAC (Scaffidi et al., 2002). This pathway is probably one of the leading mechanisms of joint dysfunction in autoimmune arthritis. If unchecked, this vicious cycle goes on to further debilitate the synovial joint tissues. It also plays an important role in tissue degeneration, neuroinflammation, and arthritis (Andersson and Erlandsson-Harris, 2004; Kim et al., 2018).

A molecular docking study showed that TXR has a high affinity towards C9, so it seems that TXR will be even more effective to cause steric hindrance resulting in the disassembly of the multimeric C9 in MAC. This may inhibit the inadvertent cellular lysis and joint damage in case of sterile inflammation or related pathogenesis (Dudkina et al., 2016). Thus, TXR may inhibit necrosis-mediated cell death by blocking C9 involvement in MAC formation. Since TXR is well tolerated, inhibition of its possible molecular targets may have minimal or no adverse effects. TXR has been widely reported to possess hepatoprotective (Zhang et al., 2017; Malinska et al., 2019) as well as renoprotective (Shan et al.,

2017) properties which can now be attributed to MAC inhibition, thus protecting the hepatic and renal cells from the xenobiotic mediated lysis. TXR is also a known antioxidant and inhibits oxidative stress-mediated cellular apoptosis (Zhang et al., 2009), and may protect the synovial joints alleviating severe damage in AIA and possibly in rheumatoid arthritis patients.

Natural products that could inhibit the production of chemokines and cytokines and modulate auto-immune crosstalk could be useful in the treatment modalities for RA. These molecules may vary through many other inflammatory mediators such as $\text{NF-}\kappa\text{B}$, MAPK, and STAT3. It can also be inferred that the effect of TXR might have resulted in the inhibition of HMGB1, thus reducing inflammation (Yang et al., 2020). The effect of TXR on the immune systems and their effector molecules needs additional studies.

The identified candidate biomarkers in responses to the drugs for RA suggest new modalities of antiarthritic treatment. However, the observations from the experimental animal model need further validation of the identified target to understand the perturbed molecular details involved in this disease pathophysiology. Understanding the molecular pathway will be useful to identify alternate druggable targets for new molecule discovery. Our results demonstrated that TXR has therapeutically beneficial effects on the experimental arthritis animal model and may be useful as a potential treatment for RA in humans after appropriate clinical trials.

In conclusion, our quantitative proteomics approach demonstrated the antiarthritic properties of a phytochemical TXR and its probable interaction with synovial proteins. A combination of quantitative proteomics studies supported by the robust protein community finding method provided a comprehensive tool to map the probable targets of TXR and its mechanism of action. The experimental approach adopted in this study will be useful at various phases of drug discovery and validation in translational studies for various disease conditions.

DATA AVAILABILITY STATEMENT

The datasets presented in this study can be found in online repositories. The names of the repository/repositories and accession number(s) can be found in the article/**Supplementary Material**.

ETHICS STATEMENT

The animal study was reviewed and approved by the Institutional Animal Ethics Committee (IAEC) of the National Institute of Immunology (NII), New Delhi (IAEC#367/15).

AUTHOR CONTRIBUTIONS

DS, AP and RN have conceptualized and designed the experiments; DS and ShiS performed the cell culture and animal experiments; DS and SB have done iTRAQ proteomics sample preparation; DS, SK, ES and ShaS performed the iTRAQ-LC MS experiment and data acquisition; DS, SK, RN,

MM, SaS and RS have done proteomics data analyses; DS, SuS, SB and RA have done proteomics validation studies; AR has done the histopathological analyses; RS has done the *in silico* study designing; DS and MM have performed the *in silico* experiments. DS, C-JL, MM and RN contributed to the writing and reviewing the manuscript.

FUNDING

The study was funded with a start-up research grant (SERB/LS-175/2014) by SERB, Government of India, in the form of DST-SERB Young Scientist Award to DS.

ACKNOWLEDGMENTS

The authors acknowledge Dr. Perumal Nagarajan and the staff of animal research facility in the National Institute of Immunology (NII), for providing support to conduct experiments. RN acknowledges core support from ICGEB, New Delhi.

SUPPLEMENTARY MATERIAL

The Supplementary Material for this article can be found online at: <https://www.frontiersin.org/articles/10.3389/fcell.2022.845457/full#supplementary-material>

Supplementary Figure 1 | (A) Schematic of iTRAQ labeling: Flowchart showing the eight-plex iTRAQ labeling and the quantitative proteomics method used for analyzing joint homogenate proteins. The iTRAQ tags 113 and 115 were used for the technical replicates of a healthy animal, while biological replicates of AIA were tagged with 114 and 116, followed by those of TXR with 117, 119 and lastly 118, 121 were used for those of DS. **(B)** One dimensional silver-stained gel shows the protein band patterns in all the study group samples.

REFERENCES

- Ali, S., Malik, M. Z., Singh, S. S., Chirom, K., Ishrat, R., and Singh, R. K. B. (2018). Exploring Novel Key Regulators in Breast Cancer Network. *PLoS One* 13, e0198525. doi:10.1371/journal.pone.0198525
- Andersson, U., and Erlandsson-Harris, H. (2004). HMGB1 Is a Potent Trigger of Arthritis. *J. Intern. Med.* 255, 344–350. doi:10.1111/j.1365-2796.2003.01303.x
- Aravilli, R. K., Vikram, S. L., and Kohila, V. (2017). Phytochemicals as Potential Antidotes for Targeting NF-Kb in Rheumatoid Arthritis. *3 Biotech.* 7, 253. doi:10.1007/s13205-017-0888-1
- Assenov, Y., Ramirez, F., Schelhorn, S.-E., Lengauer, T., and Albrecht, M. (2008). Computing Topological Parameters of Biological Networks. *Bioinformatics* 24, 282–284. doi:10.1093/bioinformatics/btm554
- Barrat, A., Barthelemy, M., Pastor-Satorras, R., and Vespignani, A. (2004). The Architecture of Complex Weighted Networks. *Proc. Natl. Acad. Sci.* 101, 3747–3752. doi:10.1073/pnas.0400087101
- Biggioggero, M., Crotti, C., Becciolini, A., and Favalli, E. G. (2019). Tocilizumab in the Treatment of Rheumatoid Arthritis: an Evidence-Based Review and Patient Selection. *Drug Des. Devel. Ther.* 13, 57–70. doi:10.2147/DDDT.S150580
- Bishwal, S. C., Das, M. K., Badireddy, V. K., Dabral, D., Das, A., Mahapatra, A. R., et al. (2019). Sputum Proteomics Reveals a Shift in Vitamin D-Binding Protein and Antimicrobial Protein Axis in Tuberculosis Patients. *Sci. Rep.* 9. doi:10.1038/s41598-018-37662-9

Supplementary Figure 2 | Scatter plots showing the correlation between the protein expressions of biological replicates in the experimental groups. Scattering plots of Pearson correlation comparing two biological replicates of iTRAQ reporter ion intensities, **(A)** AIA1 (114/113) vs. AIA2 (116/113); **(B)** DS1 (118/113) vs. DS2 (121/113); and **(C)** TXR1 (117/113) vs. TXR2 (119/113). The Pearson correlation coefficient (R2) is given for each plot.

Supplementary Figure 3 | (A) Heat map of the proteins showing both significant difference and ≥ 1.5 -fold change between the AIA and treatment groups (both DS and TXR200). **(B)** Western blot of the joint homogenate proteins of a different set of animals from each experimental group as a replicate result.

Supplementary Figure 4 | (A) Venn diagram showing four common proteins between two lists of proteins, viz., list 1 = 15 proteins (*in silico* key regulators), list 2 = 65 proteins (≥ 1.5 -fold expressed proteins between AIA and Healthy). **(B)** Venn diagram showing two common proteins between two lists of proteins, viz., list 1 = 19 proteins (≥ 1.5 -fold expressed proteins between AIA and DS) and list 2 = 17 proteins (significantly differentially expressed ($p \leq 0.05$) proteins between AIA and DS). **(C)** Venn diagram showing C9 as common among four lists of proteins, viz., list 1 = 15 proteins (*in silico* key regulators), list 2 = 65 proteins (≥ 1.5 -fold expressed proteins between AIA and healthy), list 3 = 11 proteins (≥ 1.5 -fold expressed proteins between AIA and TXR groups), and list 4 = 27 proteins (significantly differentially expressed ($p \leq 0.05$) proteins between AIA and TXR). **(D)** Venn diagram showing many sets of common proteins among five lists of proteins, viz., list 1 = 15 proteins (*in silico* key regulators), list 2 = 11 proteins (≥ 1.5 -fold expressed proteins between AIA and TXR groups), list 3 = 27 proteins (significantly differentially expressed ($p \leq 0.05$) proteins between AIA and TXR), list 4 = 19 proteins (≥ 1.5 fold expressed proteins between AIA and DS), and list 5 = 17 proteins (significantly differentially expressed ($p \leq 0.05$) proteins between AIA and DS).

Supplementary Figure 5 | Molecular docking interaction studies (molecular interaction is depicted on the left while Ligplot showing molecules involved in interactions on the right side of each column) of TXR with the proteins identified as *in silico* key regulators. **(A)** TXR with complement component 9 (C9); **(B)** TXR with catalase (Cat); **(C)** TXR with aldehyde dehydrogenase 2 (Aldh2); **(D)** TXR with phosphofruktokinase, platelet (Pfkp); **(E)** TXR with afamin (Afm); **(F)** TXR with leukotriene A4 hydrolase (LAH); **(G)** glycogenin 1 (Gyg1); **(H)** TXR with VPS29 retromer complex component (Vps29); **(I)** TXR with phosphotyrosine phosphatase inorganic pyrophosphate phosphatase (Lhpp); **(J)** TXR with protein phosphatase 1 catalytic subunit gamma (Ppp1cc); **(K)** TXR with Serpin family A member 6 (Serpina 6); **(L)** TXR with Ras-related C3 botulinum toxin substrate 1 (Rac 1); **(M)** TXR with thyrotropin-releasing hormone receptor (Trhr); **(N)** TXR with protein disulfide isomerase family A, member 3 (Pdia3); and **(O)** TXR with dihydrofolate reductase (Dhfr).

- Blondel, V. D., Guillaume, J.-L., Lambiotte, R., and Lefebvre, E. (2008). Fast Unfolding of Communities in Large Networks. *J. Stat. Mech.* 2008, P10008. doi:10.1088/1742-5468/2008/10/P10008
- Brandes, U. (2001). A Faster Algorithm for Betweenness Centrality*. *J. Math. Sociol.* 25, 163–177. doi:10.1080/0022250x.2001.9990249
- Canright, G., and Engo-Monsen, K. (2004). Roles in Networks. *Sci. Comput. Programming* 53, 195–214. doi:10.1016/j.scico.2003.12.008
- Canright, G. S., and Engo-Monsen, K. (2006). Spreading on Networks: A Topographic View. *Complexus* 3, 131–146. doi:10.1159/000094195
- Coelho, M. G. P., Reis, P. A., Gava, V. B., Marques, P. R., Gayer, C. R., Laranja, G. A. T., et al. (2004). Anti-arthritis Effect and Subacute Toxicological Evaluation of Baccharis Genistelloides Aqueous Extract. *Toxicol. Lett.* 154, 69–80. doi:10.1016/j.toxlet.2004.07.004
- Crofford, L. J. (2013). Use of NSAIDs in Treating Patients with Arthritis. *Arthritis Res. Ther.* 15, S2. doi:10.1186/ar4174
- DeLano, W. L. (2014). *The PyMOL Molecular Graphics System, Version 1.8*. New York, NY, USA: Schrödinger LLC. Available at: <http://www.pymol.org>
- Dudkina, N. V., Spicer, B. A., Reboul, C. F., Conroy, P. J., Lukoyanova, N., Elmlund, H., et al. (2016). Structure of the Poly-C9 Component of the Complement Membrane Attack Complex. *Nat. Commun.* 7. doi:10.1038/ncomms10588
- Estrada, E., and Rodríguez-Velázquez, J. A. (2005). Subgraph Centrality in Complex Networks. *Phys. Rev. E* 71. doi:10.1103/PhysRevE.71.056103
- Farooqui, A., Tazyeen, S., Ahmed, M. M., Alam, A., Ali, S., Malik, M. Z., et al. (2018). Assessment of the Key Regulatory Genes and Their Interlogs for

- Turner Syndrome Employing Network Approach. *Sci. Rep.* 8, 10091. doi:10.1038/s41598-018-28375-0
- García-Armandis, I., Guillén, M. I., Gomar, F., Pelletier, J.-P., Martel-Pelletier, J., and Alcaraz, M. J. (2010). High Mobility Group Box 1 Potentiates the Pro-inflammatory Effects of Interleukin-1 β in Osteoarthritic Synoviocytes. *Arthritis Res. Ther.* 12, R165. doi:10.1186/ar3124
- Goddard, T. D., Huang, C. C., and Ferrin, T. E. (2007). Visualizing Density Maps with UCSF Chimera. *J. Struct. Biol.* 157, 281–287. doi:10.1016/j.jsb.2006.06.010
- Guo, Q., Wang, Y., Xu, D., Nossent, J., Pavlos, N. J., and Xu, J. (2018). Rheumatoid Arthritis: Pathological Mechanisms and Modern Pharmacologic Therapies. *Bone Res.* 6. doi:10.1038/s41413-018-0016-9
- Islam, M. A., Alam, F., Solayman, M., Khalil, M. I., Kamal, M. A., and Gan, S. H. (2016). Dietary Phytochemicals: Natural Swords Combating Inflammation and Oxidation-Mediated Degenerative Diseases. *Oxidative Med. Cell Longevity* 2016, 1–25. doi:10.1155/2016/5137431
- Jannat, A., John, P., Bhatti, A., and Hayat, M. Q. (2019). Tomorrow Attenuates Progression of Rheumatoid Arthritis through Alteration in ULK-1 Independent Autophagy Pathway in Collagen Induced Arthritis Mice Model. *Cell Death Discov.* 5, 142. doi:10.1038/s41420-019-0222-2
- Kelley, N., Jeltema, D., Duan, Y., and He, Y. (2019). The NLRP3 Inflammasome: An Overview of Mechanisms of Activation and Regulation. *Ijms* 20, 3328. doi:10.3390/ijms20133328
- Kim, S. Y., Son, M., Lee, S. E., Park, I. H., Kwak, M. S., Han, M., et al. (2018). High-mobility Group Box 1-induced Complement Activation Causes Sterile Inflammation. *Front. Immunol.* 9. doi:10.3389/fimmu.2018.00705
- Lappegård, K. T., Bjerre, A., Tjønnfjord, G. E., and Mollnes, T. E. (2015). Terapeutisk Komplementhemming - Fra Eksperimentell Til Klinisk Medisin. *Tidsskr. Den Nor. Laegeforening* 135, 1745–1749.
- Li, Y., Ma, P., Fu, J., Wu, J., and Wu, X. (2019). Combining an In Silico Approach with an Animal Experiment to Investigate the Protective Effect of Troloxerutin for Treating Acute Lung Injury. *BMC Complement. Altern. Med.* 19. doi:10.1186/s12906-019-2515-7
- Malik, M. Z., Chirrom, K., Ali, S., Ishrat, R., Somvanshi, P., and Singh, R. K. B. (2019). Methodology of Predicting Novel Key Regulators in Ovarian Cancer Network: a Network Theoretical Approach. *BMC Cancer* 19. doi:10.1186/s12885-019-6309-6
- Malinska, H., Hüttel, M., Oliyarnyk, O., Markova, I., Poruba, M., Racova, Z., et al. (2019). Beneficial Effects of Troloxerutin on Metabolic Disorders in Non-obese Model of Metabolic Syndrome. *PLoS One* 14, e0220377.
- Mangangcha, I. R., Malik, M. Z., Küçük, Ö., Ali, S., and Singh, R. K. B. (2019). Identification of Key Regulators in Prostate Cancer from Gene Expression Datasets of Patients. *Sci. Rep.* 9, 16420. doi:10.1038/s41598-019-52896-x
- Markiewski, M. M., and Lambris, J. D. (2007). The Role of Complement in Inflammatory Diseases from behind the Scenes into the Spotlight. *Am. J. Pathol.* 171, 715–727. doi:10.2353/ajpath.2007.070166
- Maurya, D. K., Balakrishnan, S., Salvi, V. P., and Nair, C. K. K. (2005). Protection of Cellular DNA from γ -radiation-induced Damages and Enhancement in DNA Repair by Troloxerutin. *Mol. Cel. Biochem.* 280, 57–68. doi:10.1007/s11010-005-8052-3
- Newman, M. E. J., and Girvan, M. (2004). Finding and Evaluating Community Structure in Networks. *Phys. Rev. E* 69. doi:10.1103/PhysRevE.69.026113
- Noris, M., and Remuzzi, G. (2013). Overview of Complement Activation and Regulation. *Semin. Nephrol.* 33, 479–492. doi:10.1016/j.semnephrol.2013.08.001
- Panat, N. A., Maurya, D. K., Ghaskadbi, S. S., and Sandur, S. K. (2016). Troloxerutin, a Plant Flavonoid, Protects Cells against Oxidative Stress-Induced Cell Death through Radical Scavenging Mechanism. *Food Chem.* 194, 32–45. doi:10.1016/j.foodchem.2015.07.078
- Pastor-Satorras, R., Vázquez, A., and Vespignani, A. (2001). Dynamical and Correlation Properties of the Internet. *Phys. Rev. Lett.* 87. doi:10.1103/physrevlett.87.258701
- Ravasz, E., and Barabási, A.-L. (2003). Hierarchical Organization in Complex Networks. *Phys. Rev. E* 67. doi:10.1103/PhysRevE.67.026112
- Repasky, M. P., Shelley, M., and Friesner, R. A. (2007). *Current Protocols in Bioinformatics*. New York, NY, USA: John Wiley & Sons. vol. Chapter 8.
- Sahu, D., Raghav, S. K., Gautam, H., and Das, H. R. (2015). A Novel Coumarin Derivative, 8-methoxy Chromen-2-One Alleviates Collagen Induced Arthritis by Down Regulating Nitric Oxide, NF κ B and Proinflammatory Cytokines. *Int. Immunopharmacology* 29, 891–900. doi:10.1016/j.intimp.2015.08.012
- Sahu, D., Saroha, A., Roy, S., Das, S., Srivastava, P. S., and Das, H. R. (2012). Suramin Ameliorates Collagen Induced Arthritis. *Int. Immunopharmacology* 12, 288–293. doi:10.1016/j.intimp.2011.12.003
- Sahu, D., Sharma, S., Singla, R. K., and Panda, A. K. (2017). Antioxidant Activity and Protective Effect of Suramin against Oxidative Stress in Collagen Induced Arthritis. *Eur. J. Pharm. Sci.* 101, 125–139. doi:10.1016/j.ejps.2017.02.013
- Sarin, S. K., Kedarisetty, C. K., Kedarisetty, C. K., Abbas, Z., Amarapurkar, D., Bihari, C., et al. (2014). Acute-on-chronic Liver Failure: Consensus Recommendations of the Asian Pacific Association for the Study of the Liver (APASL) 2014. *Hepatol. Int.* 8, 453–471. doi:10.1007/s12072-014-9580-2
- Scaffidi, P., Misteli, T., and Bianchi, M. E. (2002). Release of Chromatin Protein HMGB1 by Necrotic Cells Triggers Inflammation. *Nature* 418, 191–195. doi:10.1038/nature00858
- Seeuws, S., Jacques, P., Van Praet, J., Drennan, M., Coudensys, J., Decruy, T., et al. (2010). A Multiparameter Approach to Monitor Disease Activity in Collagen-Induced Arthritis. *Arthritis Res. Ther.* 12, R160. doi:10.1186/ar3119
- Serada, S., Fujimoto, M., Ogata, A., Terabe, F., Hirano, T., Iijima, H., et al. (2010). iTRAQ-Based Proteomic Identification of Leucine-Rich -2 Glycoprotein as a Novel Inflammatory Biomarker in Autoimmune Diseases. *Ann. Rheum. Dis.* 69, 770–774. doi:10.1136/ard.2009.118919
- Shan, Q., Zheng, G. H., Han, X. R., Wen, X., Wang, S., Li, M. Q., et al. (2018). Troloxerutin Protects Kidney Tissue against BDE-47-Induced Inflammatory Damage through CXCR4-Txnip/nlrp3 Signaling. *Oxid. Med. Cel. Longev.* 2018, 9865495. doi:10.1155/2018/9865495
- Shan, Q., Zhuang, J., Zheng, G., Zhang, Z., Zhang, Y., Lu, J., et al. (2017). Troloxerutin Reduces Kidney Damage against BDE-47-Induced Apoptosis via Inhibiting NOX2 Activity and Increasing Nrf2 Activity. *Oxidative Med. Cell Longevity* 2017, 1–12. doi:10.1155/2017/6034692
- Shannon, P., Markiel, A., Ozier, O., Baliga, N. S., Wang, J. T., Ramage, D., et al. (2003). Cytoscape: A Software Environment for Integrated Models of Biomolecular Interaction Networks. *Genome Res.* 13, 2498–2504. doi:10.1101/gr.1239303
- Sharma, S., Sahu, D., Das, H. R., and Sharma, D. (2011). Amelioration of Collagen-Induced Arthritis by Salix Nigra Bark Extract via Suppression of Pro-inflammatory Cytokines and Oxidative Stress. *Food Chem. Toxicol.* 49, 3395–3406. doi:10.1016/j.fct.2011.08.013
- Tang, Y., Li, M., Wang, J., Pan, Y., and Wu, F.-X. (2015). CytoNCA: a Cytoscape Plugin for Centrality Analysis and Evaluation of Protein Interaction Networks. *Biosystems* 127, 67–72. doi:10.1016/j.biosystems.2014.11.005
- Tarantino, G., Minno, M. N. D. D., and Capone, D. (2009). Drug-induced Liver Injury: Is it Somehow Foreseeable? *Wjg* 15, 2817–2833. doi:10.3748/wjg.15.2817
- Thomas, N. S., George, K., Arivalagan, S., Mani, V., Siddique, A. I., and Namasivayam, N. (2017). The In Vivo Antineoplastic and Therapeutic Efficacy of Troloxerutin on Rat Preneoplastic Liver: Biochemical, Histological and Cellular Aspects. *Eur. J. Nutr.* 56, 2353–2366. doi:10.1007/s00394-016-1275-0
- Ungurte, A., Bernotiene, E., Bagdonas, E., Garberyste, S., Porvaneckas, N., and Jorgensen, C. (2016). Human Articular Chondrocytes with Higher Aldehyde Dehydrogenase Activity Have Stronger Expression of COL2A1 and SOX9. *Osteoarthritis and Cartilage* 24, 873–882. doi:10.1016/j.joca.2015.11.019
- Urushima, H., Fujimoto, M., Mishima, T., Ohkawara, T., Honda, H., Lee, H., et al. (2017). Leucine-rich Alpha 2 Glycoprotein Promotes Th17 Differentiation and Collagen-Induced Arthritis in Mice through Enhancement of TGF- β -Smad2 Signaling in Naïve Helper T Cells. *Arthritis Res. Ther.* 19, 137. doi:10.1186/s13075-017-1349-2
- Warde-Farley, D., Donaldson, S. L., Comes, O., Zuberi, K., Badrawi, R., Chao, P., et al. (2010). The GeneMANIA Prediction Server: Biological Network Integration for Gene Prioritization and Predicting Gene Function. *Nucleic Acids Res.* 38, W214–W220. doi:10.1093/nar/gkq537
- Yang, H., Wang, H., and Andersson, U. (2020). Targeting Inflammation Driven by HMGB1. *Front. Immunol.* 11, 484. doi:10.3389/fimmu.2020.00484
- Yang, J., Yan, R., Roy, A., Xu, D., Poisson, J., and Zhang, Y. (2014). The I-TASSER Suite: Protein Structure and Function Prediction. *Nat. Methods* 12, 7–8. doi:10.1038/nmeth.3213
- Yeger-Lotem, E., Sattath, S., Kashtan, N., Itzkovitz, S., Milo, R., Pinter, R. Y., et al. (2004). Network Motifs in Integrated Cellular Networks of Transcription-

- Regulation and Protein-Protein Interaction. *Proc. Natl. Acad. Sci.* 101, 5934–5939. doi:10.1073/pnas.0306752101
- Zhang, Z.-f., Fan, S.-h., Zheng, Y.-l., Lu, J., Wu, D.-m., Shan, Q., et al. (2009). Troloxerutin Protects the Mouse Liver against Oxidative Stress-Mediated Injury Induced By D-Galactose. *J. Agric. Food Chem.* 57, 7731–7736. doi:10.1021/jf9012357
- Zhang, Z.-F., Shan, Q., Zhuang, J., Zhang, Y.-Q., Wang, X., Fan, S.-H., et al. (2015). Troloxerutin Inhibits 2,2',4,4'-tetrabromodiphenyl Ether (BDE-47)-Induced Hepatocyte Apoptosis by Restoring Proteasome Function. *Toxicol. Lett.* 233, 246–257. doi:10.1016/j.toxlet.2015.01.017
- Zhang, Z.-F., Zhang, Y.-Q., Fan, S.-H., Zhuang, J., Zheng, Y.-L., Lu, J., et al. (2015). Troloxerutin Protects against 2,2',4,4'-tetrabromodiphenyl Ether (BDE-47)-Induced Liver Inflammation by Attenuating Oxidative Stress-Mediated NAD⁺-depletion. *J. Hazard. Mater.* 283, 98–109. doi:10.1016/j.jhazmat.2014.09.012
- Zhang, Z., Wang, X., Zheng, G., Shan, Q., Lu, J., Fan, S., et al. (2017). Troloxerutin Attenuates Enhancement of Hepatic Gluconeogenesis by Inhibiting NOD Activation-Mediated Inflammation in High-Fat Diet-Treated Mice. *Int. J. Mol. Sci.* 18, 31. doi:10.3390/ijms18010031

Conflict of Interest: The authors declare that the research was conducted in the absence of any commercial or financial relationships that could be construed as a potential conflict of interest.

Publisher's Note: All claims expressed in this article are solely those of the authors and do not necessarily represent those of their affiliated organizations, or those of the publisher, the editors, and the reviewers. Any product that may be evaluated in this article, or claim that may be made by its manufacturer, is not guaranteed or endorsed by the publisher.

Copyright © 2022 Sahu, Bishwal, Malik, Sahu, Kaushik, Sharma, Saini, Arya, Rastogi, Sharma, Sen, Singh, Liu, Nanda and Panda. This is an open-access article distributed under the terms of the Creative Commons Attribution License (CC BY). The use, distribution or reproduction in other forums is permitted, provided the original author(s) and the copyright owner(s) are credited and that the original publication in this journal is cited, in accordance with accepted academic practice. No use, distribution or reproduction is permitted which does not comply with these terms.